RESEARCH PAPER

Residual stress relaxation in HFMI-treated fillet welds after single overload peaks

Jan Schubnell[1] · Eva Carl[1] · Majid Farajian[1] · Stefanos Gkatzogiannis[2] · Peter Knödel[2] · Thomas Ummenhofer[2] · Robert Wimpory[3] · Hamdollah Eslami[4]

Abstract

The induction of near-surface compressive residual stress is an important factor for fatigue life improvement of HFMI-treated welded joints. However, the relaxation of these beneficial residual stresses under single overload peaks under variable amplitude and service loads may significantly reduce fatigue life improvement. For this reason, several recommendations exist to limit the maximum applied load stress for this kind of post-treated welded joints. In this work, the effect of single tension and compression overloads on the relaxation behavior of HFMI-induced residual stresses was studied experimentally by means of X-ray and neutron diffraction techniques complemented by numerical simulation at transverse stiffeners made of mild S355J2 steel and high strength S960QL steel. Loads were applied close to the real yield strength of the base material. Significantly different relaxation behavior was observed for S355J2 and S960QL steel. Furthermore, high compression loads lead to full residual stress relaxation at the weld toe of S960QL and moderate relaxation for S355J2. High tension loads lead only to slight relaxation.

Keywords High Frequency Mechanical Impact · Residual Stress Relaxation · X-ray Neutron Diffraction Technique · Finite Element Simulation

1 Introduction

High-frequency mechanical impact (HFMI) is a user-friendly and effective post-weld surface treatment method for improving the fatigue strength of welded steel joints and components. It is assumed that this improvement is strongly related to the induction of near-surface compressive residual stress but also to a decrease of the stress concentration factor (SCF) at the weld toe and the work hardening effect. A significant fatigue life improvement is statistically proved by numerous experimental studies for a wide range of steel grades summarized in the IIW Recommendation from 2016 [1]. In this document the fatigue strength improvement (increase of FAT classes) depends on the base material, weld detail, and load ratio (R). However, this recommendation is based on numerous fatigue tests performed under constant amplitude (CA) loading. Further investigations under variable amplitude (VA) loading that is more related to industrial applications revealed that the fatigue life improvement might decrease significantly for both mild and high strength steel [2, 3].

As mentioned, the benefit of the HFMI treatment is related to compressive residual stresses. However, they can relax under high mean stresses and single stress peaks if the sum of residual stress and load stress exceeds the local material yield strength [4]. For this reason, a reduction in the number of FAT classes with respect to the stress ration of $R > 0.15$ up to $R = 0.52$ was proposed by Marquis et al. [5] and transferred to the IIW Recommendation [1]. Furthermore, the IIW Recommendation for post weld treatment methods [6] limits the allowable stress for hammer and needle peened joints to $0.8f_y$, where f_y is the base material nominal yield strength. As well, the allowable stress ratio was limited to $R = 0.5$. In the current IIW recommendation, the nominal maximum stress range $\Delta S_{max} = 0.9f_y$, which corresponds to a maximum

✉ Jan Schubnell
jan.schubnell@iwm.fraunhofer.de

[1] Fraunhofer Institute for Mechanics of Materials (IWM), Freiburg, Germany

[2] Steel & Lightweight Structures, Karlsruhe Institute of Technology (KIT), Karlsruhe, Germany

[3] Helmholtz-Zentrum Berlin (HZB), Berlin, Germany

[4] Institute of Joining and Welding (IFS), University of Braunschweig, Braunschweig, Germany

⌖ Springer

compressive stress of $S_{max} = -0.45f_y$, was set as limit for $R = -1$. Mikkola et al. [7] proposed a value of $R = 0.7$ as maximum stress ratio for $\Delta S_{max} = 1.2f_y$, which corresponds to a maximum compressive stress for $S_{max} = -0.6f_y$ as maximum allowable stress of $R < -0.5$. Furthermore, for the development of the new German DASt-guideline (German Association of Steel Construction) [8], the stress range is limited to $\Delta S_{max} = 1.5f_y$, and the maximum stresses are limited to $S_{max} = -0.8f_y$ for compressive and to $S_{max} = f_y$ for tensile load.

The mentioned recommendations support the assumption that the stability of beneficial compressive residual stresses is an important factor in the fatigue behavior of HFMI-treated welded joints. According to further investigations of HFMI-treated welded joints under VA loading [9, 10] it is expected that single stress peaks, as single incidents or as part of service loading, might reduce the HFMI treatment benefits partly. Therefore, compressive loads tend to relax compressive residual stresses in proportion to their magnitude [11]. Furthermore, tensile loads may result in changing the self-equilibrated tensile residual stress deeper in the material and lead also to a relaxation of the compressive residual stress. However, only the draft of the German DASt-guideline [8] distinguishes between compressive and tensile load.

Further experimental studies on the residual stress relaxation of welded joints show that the main residual stress relaxation occurs during the very first load cycle [12]. Similar relaxation behavior was also observed by Leitner et al. [13]. This leads to the conclusion that it is crucial to investigate the effect of overload peaks under VA loading by single quasi-static loads. In this work, single loads were applied on HFMI-treated transverse stiffeners made of mild and high strength steel. The resulting residual stress relaxation was determined experimentally and numerically. The effect of load direction (tensile/compression) was investigated.

2 Experimental test setup

Two commonly used steel grades were investigated with significant different mechanical properties. As mild, structural, cold-rolled steel, S355J2+N in normalized condition with a real yield of $f_{y, real} = 420$ MPa was used. Additionally, one high strength steel S960QL with real yield strength of 1011 MPa was used for this work. The chemical compositions of the base materials and filler materials are shown in Table 1, and the mechanical properties are given in Table 2.

In this work, the investigated fillet welds were manufactured with a metal active gas (MAG) welding process. The weld detail was a double-sided transverse stiffener, shown in Fig. 1a. The manufacturing of each welded joint was performed by the aid of a welding robot. Welding parameters and manufacturing details are given by Schubnell et al. [14]. The specimens were treated with the HFMI-device Pitec weld line 10. Working pressure was 6 bars, and hammering frequency was 90 Hz. The treatment results are shown in Fig. 1.

Nominal stress S_{max} was applied on the specimen until $S_{max} = \pm 0.75 f_{y, real}$, respectively, $S_{max} = \pm 0.9 f_{y, real}$ at different specimens, where $f_{y, real}$ is the real yield of the base materials given in Table 2. The lower load levels are motivated by fatigue test results of HFMI-treated welded joints under VA loading summarized by Mikkola et al. [7], where $0.76f_y$ was the maximum applied load peak. The higher load level is motivated by a validation of the recommended maximum stress of $S_{max} = -0.8f_y$ [8]. For loading, a servo-hydraulic testing machine PLm630n was used, shown in Fig. 1b.

3 Experimental residual stress analysis

The surface residual stresses were determined by X-ray diffraction with Cr-Kα-radiation at the ferritic {211}-lattice plane. The collimator diameter was 2.0 mm. The measurements were performed under 11 ψ angles (13°, 18°, 24°, 27°, 30°, 33°, 36°, 39°, 42°, 45°, and 48°) under a 2θ range from 149 to 163°. Former measurements [15] revealed that the compressive residual stress maximum is not located in the center of the HFMI-treated groove after treatment. For this reason, the measurements for each specimen were performed from the center of the notch root perpendicular to the treatment direction until the maximum of the transverse residual stresses were found. The residual stress evaluation was performed with the sin²ψ-method. For this the elastic constants $-1/2\ S_2 = 6.08 \times 10^{-6}$ mm²/N were used. The results of the X-ray measurements are illustrated in Fig. 2.

The neutron measurements were carried out on residual stress diffractometer E3 at the Helmholtz-Zentrum Berlin [16]. The measurement setup is shown in Fig. 3b and c. A gauge volume of $2 \times 2 \times 2$ mm³ was used for the longitudinal and normal principal strain directions and a gauge volume of $5 \times 2 \times 2$ mm³ for the transverse principal strain direction, where 5 mm is the height of the input slit. The input slit was used for the primary neutron optics and an oscillating radial collimator for the secondary optic. The ferritic {211} Bragg peak was measured using a neutron wavelength of 0.147 nm. This meant that the resulting scattering angle was ~2θ = 78.85°.

For the measurements near the surface, the instrumental gauge volume (IGV) is not fully immersed. This can lead to a detected shift (aberration) of the Bragg peak which is not related to strain [17]. This so-called surface effect can be mitigated using different techniques: For the out of plane normal strain direction, the bending radius of the Si [400] monochromator is set fortuitously, so the surface effect could be eliminated [18]. For the longitudinal and transverse directions, strain measurements were measured twice, 180° to each other. This is because the shift of the Bragg peak due to the surface

Table 1 Chemical composition of the investigated base materials determined by spectral analysis

Materials	Elements (wt%) (Fe = bal.)												
	C	Mn	Si	P	S	Cr	Ni	Mo	V	W	Cu	Al	Ti
S355J2	0.161	1.47	0.17	0.0107	0.0053	0.040	0.035	0.007	0.008	0.004	0.015	0.032	0.0125
S960QL	0.155	1.23	0.206	0.0095	0.0017	0.194	0.084	0.599	0.046	0.007	0.013	0.057	0.003
G4Si1*	0.09	1.7	0.9	0.015	0.010						0.05		
Mn4Ni2CrMo**	0.1	1.8	0.8			0.35	2.3	0.6					

*Data sheet according to EN ISO 14341-A

**Data sheet according to EN ISO 16834-A (Union X90)

effect is symmetrical and numerically cancels out when adding the 180° pairs of measurements [19]. Diffraction elastic constants of E211 = 220 GPa and E211 = 0.28 [20] were used to convert strain into stress using Hooke's law.

Due a gradient of microstructure in the heat affected zone (HAZ), mostly residual stress-free specimens were used as reference, so-called d0-specimen, shown in Fig. 2a. These d0-specimens were manufactured from the same welded joint by EDM cutting [21]. The results of the neutron diffraction measurements are reported in Sect. 4.

4 Numerical study

For this study, the finite element (FE) models developed by Hardenacke et al. [22] were used. The models were stepwise improved by Foehrenbach et al. [23] and, later, by [24] and Ernould et al. [25]. For all simulations a fully dynamic model was used (Abaqus© Explicit solver).

The vertical pin movement in the FE model was controlled with a reference force with variable amplitude by a so-called VUAMP subroutine (vectorized amplitude) implemented [26]. As input for this subroutine, an impact period from a PIT device was used [25]. The pin movement in Z-direction is given by a so-called VDISP subroutine (vectorized displacement). The input for the routine is the step time of the simulation. The routine moves the pin to the impact position if the vertical pin position reaches its initial location. This ensures that the pin does not move until it is in contact with the material. A maximum of 424 impacts in 33 mm was calculated. This corresponds to a feed rate of 7 mm/s.

The process is modelled in an FE half model with a symmetric plane of the y- and z-axis, shown in Fig. 4. The mesh of the model involves 290608 8-node continuum elements with reduced integration and hourglass control (C3D8R) with a minimum mesh size of 125 μm that is recommended by Hardenacke et al. [22].

The complex geometry of the weld toe and, thus, the complex contact between the hammer pin and welded joint were also taken into account in this approach. For this, the surface was digitalized by a 3D laser measurement system and stepwise translated in a 2D surface, 3D volume, and 3D mesh model [27]. Details of the measurement system and of this procedure for 2D models are given by Schubnell et al. [28].

To model the complex material behavior for the HFMI treatment process, a so-called VUMAT subroutine (vectorized user material [29]) was written by Maciolek [30] and slightly extended the widespread, combined isotropic-kinematic hardening model according to Chaboche [31] and Chaboche [32]. For this model, the von Mises yield criterion is used. The

Table 2 Mechanical properties of the investigated base materials

Materials	Real yield strength [MPa]	Ultimate strength [MPa]	Elongation [%]	Hardness [HV10]	Generic name
S355J2+N	420	538	25***	169	-
S960QL	1011	1060	14***	316	Strenx S960E
G4Si1*	> 460	> 560	29	-	-
Mn4Ni2CrMo**	> 890	> 940	> 15	-	Union X90

*Data sheet according to EN ISO 14341-A

**Data sheet according to EN ISO 16834-A (Union X90)

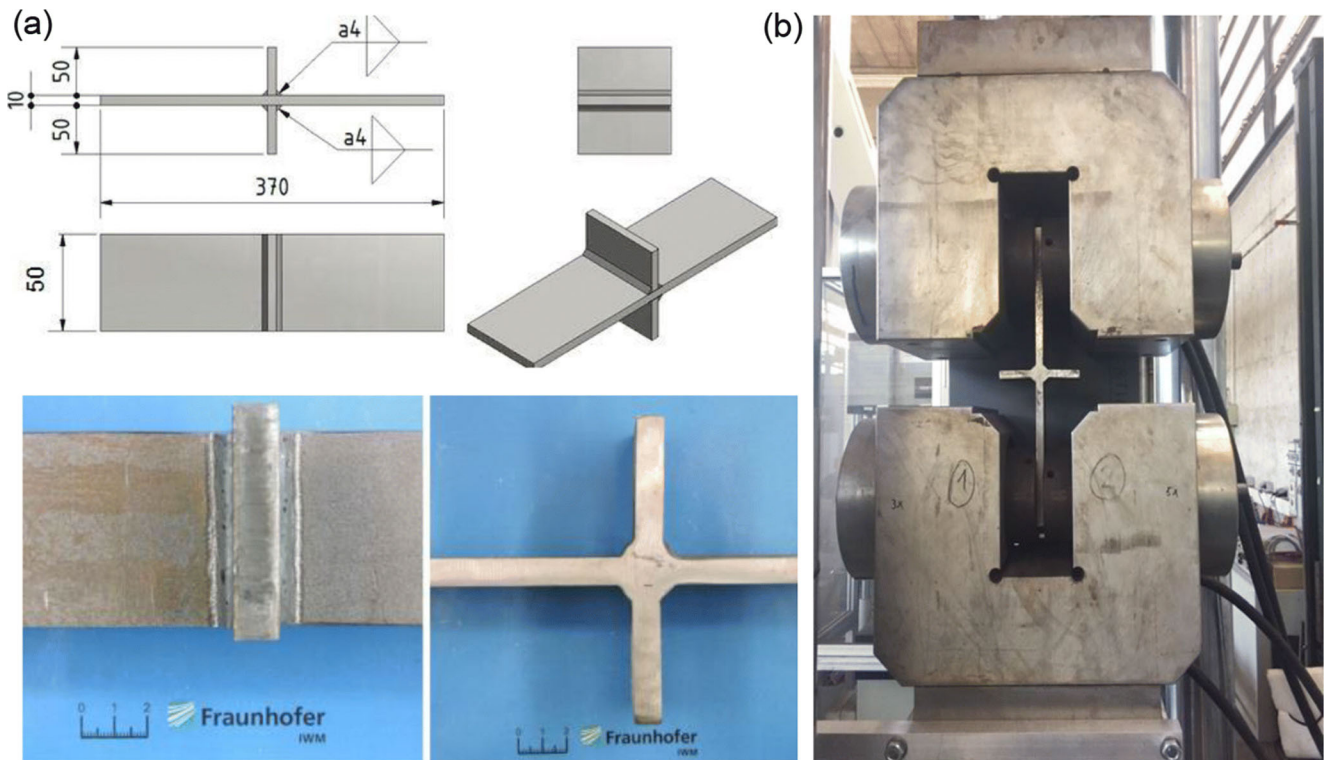***Data sheet (delivery condition according to EN 10025)

Fig. 1 **a** Specimens technical drawing and specimen picture. **b** Specimen in servo-hydraulic test rig for overload test
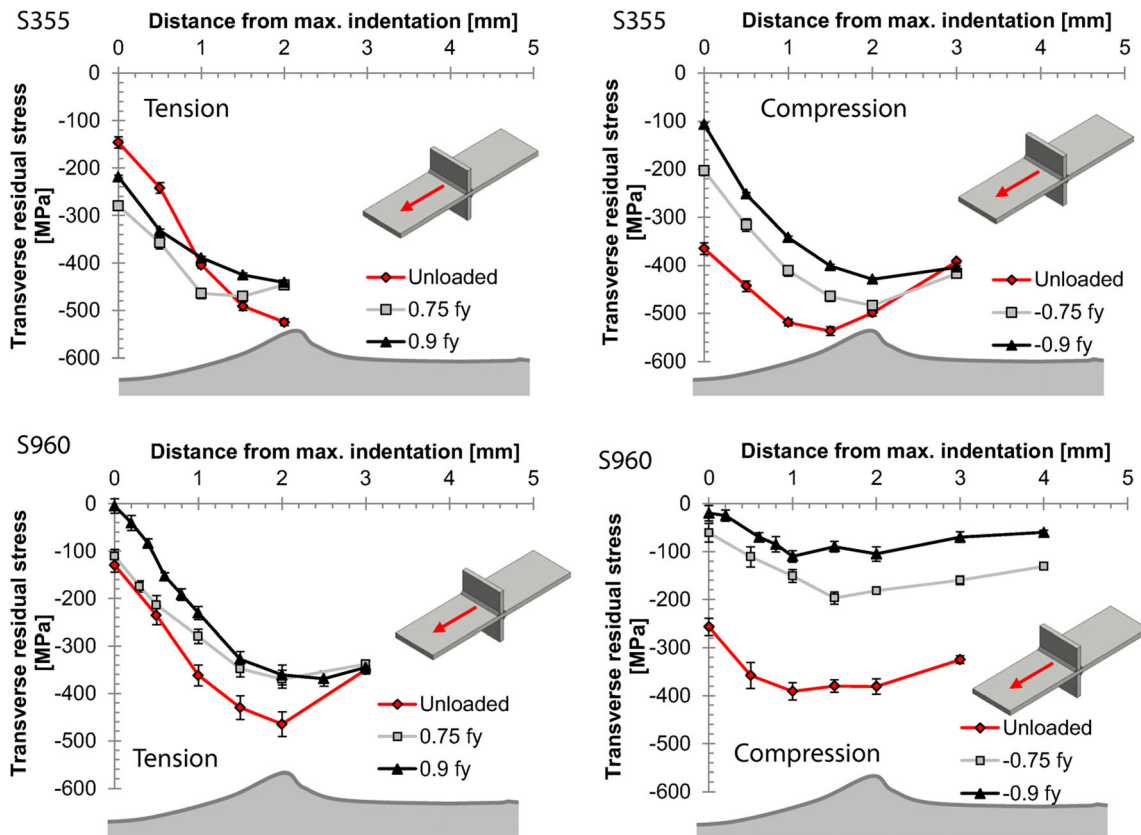

Fig. 2 Transverse residual stress state at the root of the HFMI-treated groove after treatment and after loading
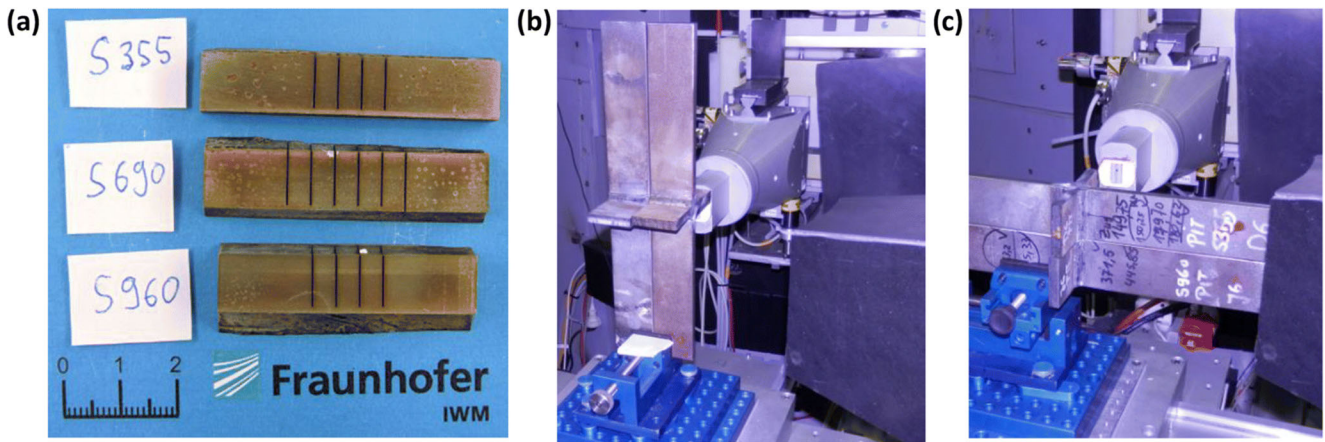
Fig. 3 Neutron diffraction RS analysis; **a** d0-specimen, **b** measurement setup for normal and longitudinal direction, and **c** measurement setup for transverse direction

isotropic part of the model is based on the evolution term of Zaverl and Lee [33]:

$$\dot{k} = m(k_1 - k)\, \dot{\varepsilon}^p \qquad (1)$$

where m and k_1 are material parameters and $\dot{\varepsilon}^p$ is the time derivative of the plastic strain tensor. This equation can be solved analytically by time integration:

$$k = k_1 - (k_1 - k_0) \exp\left(-m\, \overline{\varepsilon}_{eq}^p\right). \qquad (2)$$

where k_0 is the initial yield surface and $\dot{\overline{\varepsilon}}_{eq}^p$ is the equivalent plastic strain rate. As modification of the original model, the yield surface k was split into two parts k_k for a better modelling of the isotropic hardening as suggested by Chaboche [34] and modelled by Erz et al. [35]. This extends k to
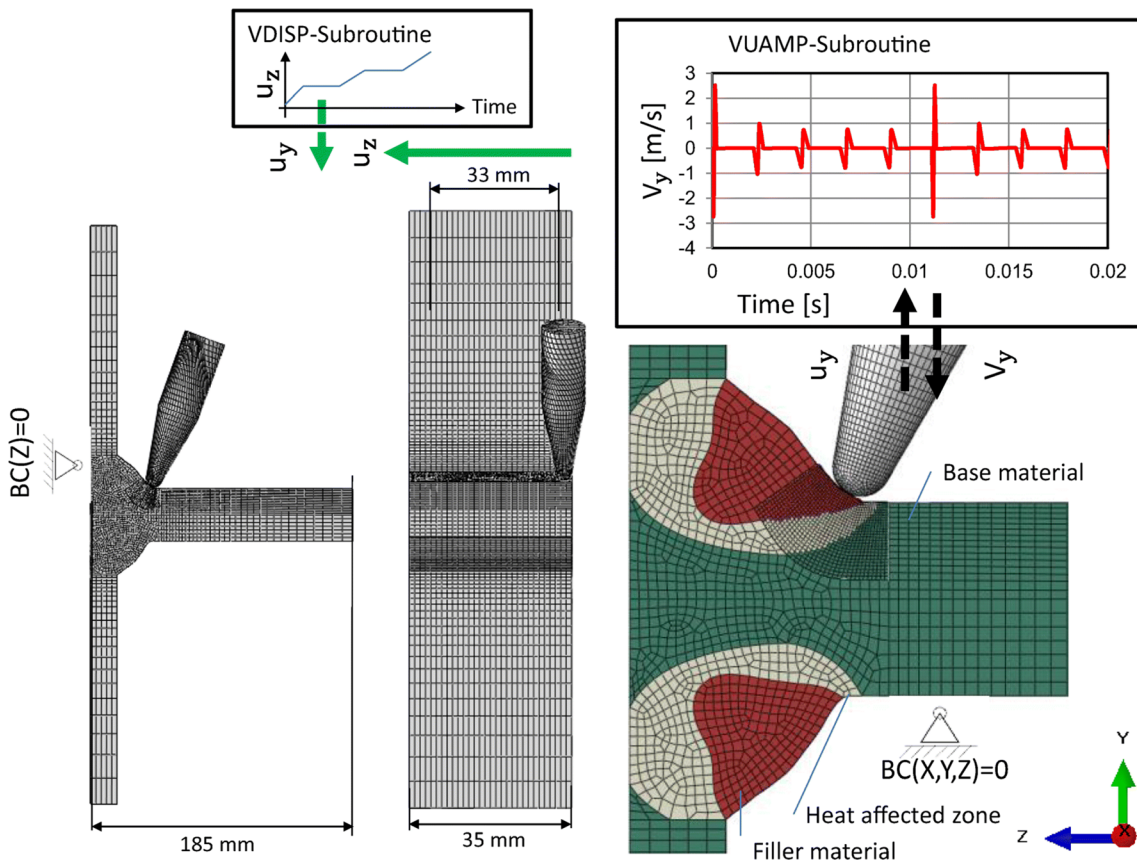

Fig. 4 Finite element (FE) model for HFMI simulation of transverse stiffener

$$\dot{k}_k = m_k\left(k_{k,1}-k\right)\dot{\varepsilon}^p_{eq} \quad \text{with} \quad k = \sum_{k=1}^{n} k_k \tag{3}$$

The kinematic term Ω is split into multiple backstress terms:

$$\Omega = \sum_{k=1}^{n} \Omega_k \tag{4}$$

Chaboche [34] suggests two backstress terms Ω_1 and Ω_2 with the evaluation term according to Armstrong and Frederick [36] described in detail in Frederick and Armstrong [37] with the material parameter C_k and γ_k for each term:

$$\dot{\Omega}_k = \frac{2}{3}C_k\dot{\varepsilon}^p - \gamma_k\Omega_k\dot{\varepsilon}^p_{eq} \tag{5}$$

For the case of uniaxial loading, the stress can be calculated by the simplified equations:

$$|\,\sigma - \Omega_1 + \Omega_2\,| \geq k \tag{6}$$

$$\sigma = \Omega_1 + \Omega_2 + \kappa K + \kappa K\left(\dot{\varepsilon}^p\kappa\right)^{\frac{1}{n}} \tag{7}$$

$$\kappa = \frac{\sigma - \Omega_1 - \Omega_2}{|\sigma - \Omega_1 - \Omega_2|} = \begin{cases} 1, & \text{tensile load} \\ 1, & \text{compressive load} \end{cases} \tag{8}$$

where Ω_1 and Ω_2 are the backstress terms, k_0 is the initial yield surface, and residual term is the strain-dependent part of the flow stress with the material parameters K and n.

Former studies have shown a strong effect of back stress (Bauschinger effect) on the residual stress state after HFMI treatment of S355 and S960 steel [23]. To cover this effect, strain-controlled tension-compression tests at different constant strain amplitudes were used to determine the cyclic stress-strain behavior shown in Fig. 5. The constitutive model was calibrated by single-element calculations according to the first three load cycles, similar to former studies by Föhrenbach et al. [23] and Ernould et al. [38].

The change of the mechanical properties due to recrystallization and phase transformation by heating and cooling during the welding process was also taken into account in this work. For this, the HAZ microstructure was thermophysically simulated with a Gleeble 3150 simulator by Schubnell et al. [14]. The hardness and microstructure of this simulated HAZ showed a very good agreement with the original HAZ. The cyclic stress-strain behavior of HAZ differs significantly from that of the base material for S355J2+N. However, minor differences were observed for the HAZ and base material of S960QL.

For the constitutive modelling of filler material, the commercial software package JMatPro© Version 10 was used. With this software package, the mechanical properties were interpolated based on the ThermoTech database [39]. As

input, the chemical compositions from the data sheet were used, given in Table 1. The isotropic stress-strain behavior is shown in Fig. 5.

For the fit of the constitutive model, the Young's modulus E was set to 210 GPa, and the Poisson's ratio ν was set to 0.3. The strain rate dependency of the model (parameter κ and n) was fitted according to high speed tensile tests with a nominal strain rate in a range from 0.001 1/s to 500 1/s [14]. For the fitting of the kinematic and isotropic terms of the model, a maximum of three parameters were used for the fitting, according to the recommended order of Maciolek [28]. The parameters for the hardening model are summarized in Table 3.

Welding residual stresses were included as initial stress condition in this analysis [40], shown in the contour plot in Fig. 6. However, the welding residual stresses in transverse direction reached between 0 and − 50 MPa for both base materials. Higher transverse residual stresses around 550 MPa for S960QL and around 300 MPa for S355J2 were observed below the surface around transition of HAZ and heat-unaffected base material.

The resulting residual stress fields of the FE simulation are illustrated in Fig. 6. As shown, the welding residual stresses in the model were only affected around the treated weld toe and in a depth of around 2 mm. In a case of a tensile overload (+ 0.9 f_y), compressive residual stresses do not fully relax for S960QL. However, in the case of a compressive overload (− 0.9 f_y), compressive residual stresses were almost eliminated for S960QL. Similar behavior was observed for S355J2. However, in this case no full relaxation was shown for high compressive loads (− 0.9f_y).

The residual stress depth profiles in transverse and longitudinal direction are shown in Fig. 7 for S355J2 and in Fig. 8 for S960QL. The residual stress profiles from FE simulation were evaluated in the middle of the model (X-direction) and in the middle of the HFMI-treated groove (Z-direction). The stress values were averaged over an identical measurement volume ($2 \times 2 \times 2$ mm^3) in depth according to the neutron diffraction measurements. At the surface the stresses were averaged over an identical area like the performed X-ray measurements.

The numerical and experimental determined residual stress profiles in transverse direction show a compression maximum of around −400 MPa (Exp.) to − 460 MPa (Sim.) for S960QL in a depth of 0.25 mm (Exp.) to 0.5 mm (Sim.) for S960QL. For S355J2 a maximum of compressive residual stress of around − 280 MPa was observed. Compared with the measurements, the simulation tends to overestimate the HFMI-induced residual stresses values slightly and underestimates the indentation in longitudinal direction.

For S355J2 only minor residual stress relaxation of 50 MPa was observed for the compressive residual stress maximum in transverse direction at 0.9f_y, shown in Fig. 7. For a load with − 0.9 f_y, a residual stress relaxation of 110 MPa was observed.
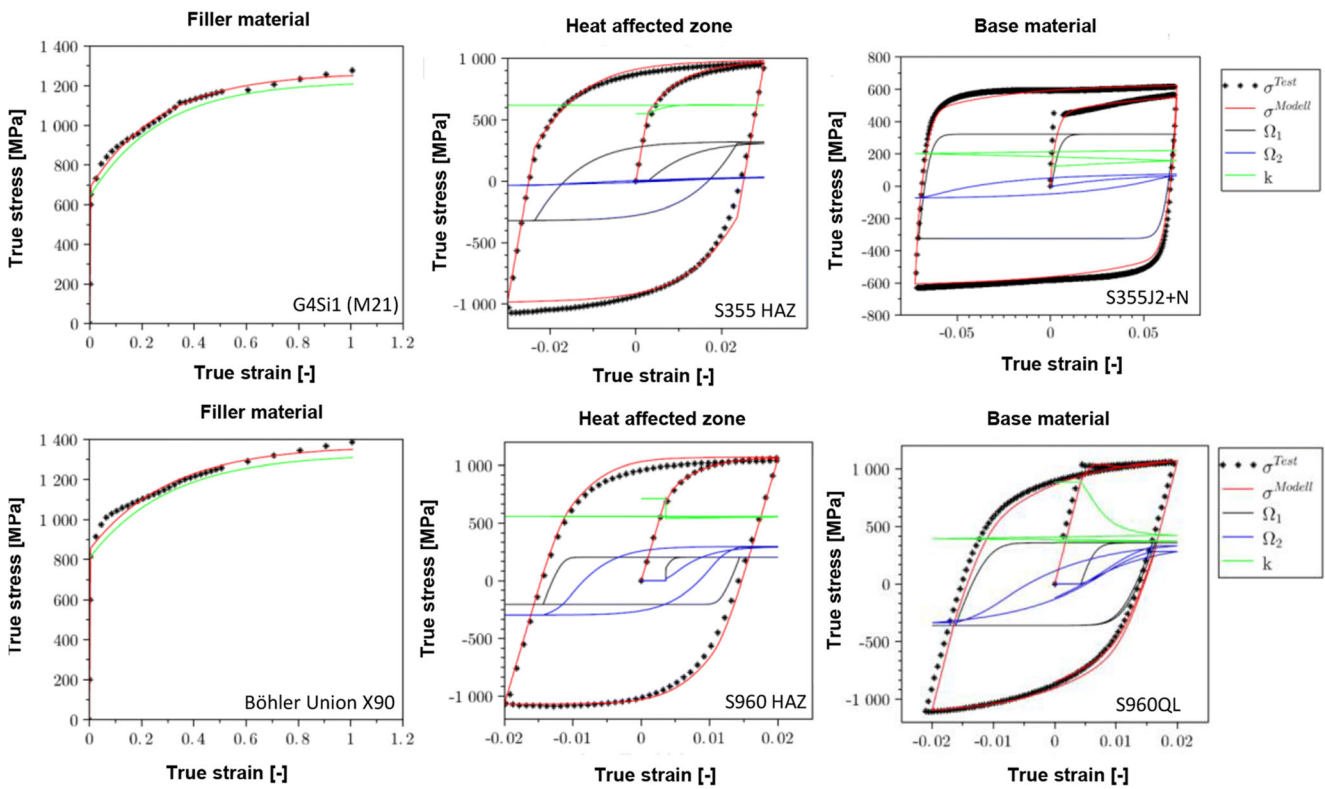
Fig. 5 Calibration of the constitutive model according to experimental data

However, a significant difference of the residual stress depth profiles after tensile and compressive loading was observed for S960QL, illustrated in Fig. 8. The numerically determined residual stress profiles after $0.45f_y$, $0.6f_y$, $0.75f_y$, and $0.9f_y$ load show only slight differences. However, in each of the mentioned load cases, a relaxation of around 80 MPa compared with the initial residual stress state was observed. Under compression $(0.9f_y)$ nearly full RS relaxation was observed by the numerical simulation similar to the experimental results for S960QL. Furthermore, a significant relaxation of -200 MPa was observed for a moderate load of $0.45 f_y$.

5 Discussion

The compressive residual stresses at the surface and their gradient through the depth to the maximum are important factors for fatigue analysis for fracture mechanics concepts [41] and the approaches of local fatigue assessment [42, 43]. Therefore, the relaxation of the surface residual stresses and the compression residual stress maximum below the surface was evaluated, illustrated in Fig. 9. As shown, nearly full relaxation was observed for S960QL specimens under the highest applied compressive load $(-0.9 f_{y, real})$. However, at the same normalized load level, comparably less residual stress relaxation was observed for S355J2. This could be explained by the similar mechanical properties at the HAZ for both materials that lead to a significant lower ratio of local stress and yield for S355, shown in Fig. 5.

Experimental and numerical investigations show that significant relaxation occurs at the investigated weld type for maximum allowable compressive loads of $-0.8 f_{y, real}$, validating the previous study by Kuhlmann et al. [8], especially for S960QL. Furthermore, for S960QL nearly half of the

Table 3 Parameters for the elasto-viscoplastic constitutive model for base material (BM) and heat affected zone (HAZ)

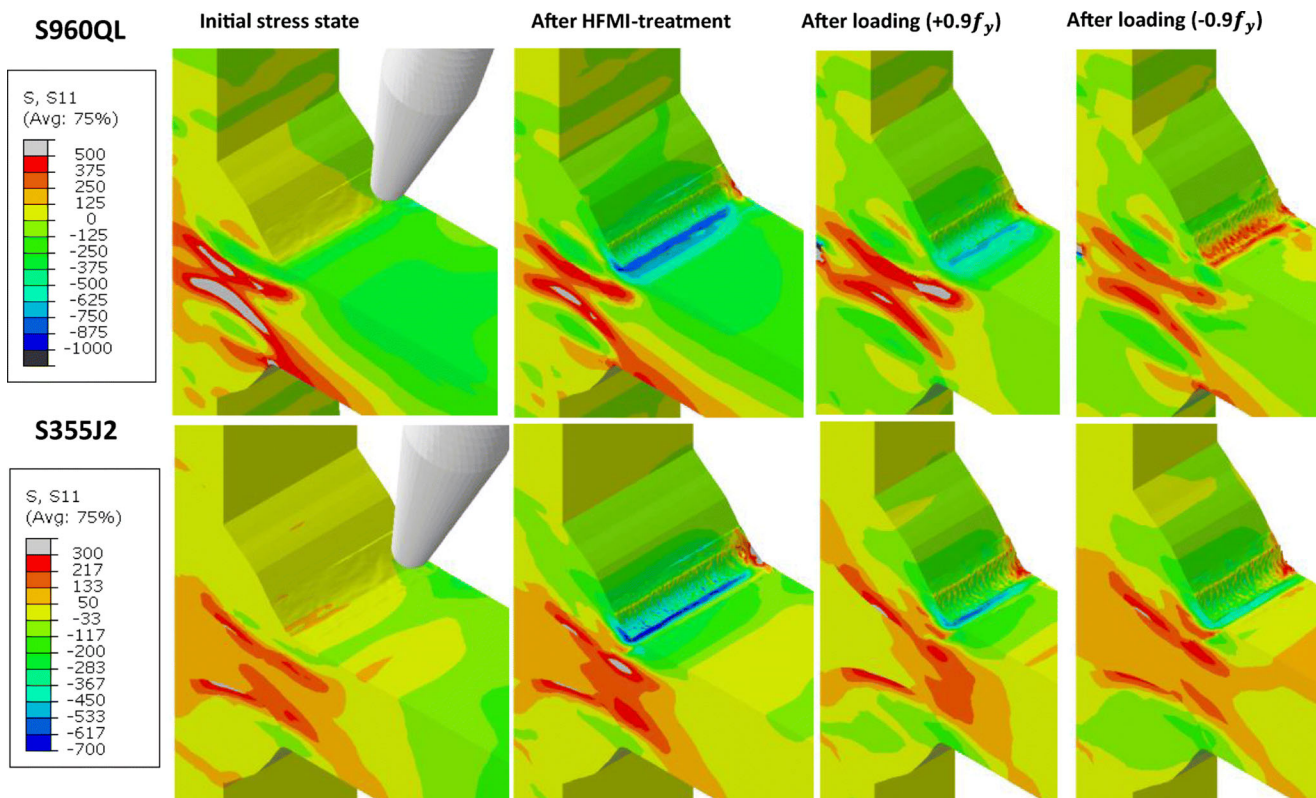| Parameter	k_{10}	k_{11}	k_{20}	k_{21}	m_1	m_2	C_1	C_2	γ_1	γ_2	κ	n
Unit	[MPa]	[MPa]	[MPa]	[MPa]	[-]	[-]	[MPa]	[MPa]	[-]	[-]	[MPa]	[-]
S355J2 BM	92	219.1	328	-29.8	28.5	309	130,000	402	402	25	13.4	2.04
S355J2 HAZ	300	659	251	-39.6	234	202	41,457	1554	128.9	1554	71.62	3.49
S960QL BM	682.9	228	202.9	17.582	312	5.11	317,476	34,919	883	92	105	3.73
S960QL HAZ	512.8	529	201	28.1	77.6	529	707,050	85,158	3476	287	92.2	3.49

Fig. 6 Contour plot of transverse residual stress state at different simulation steps
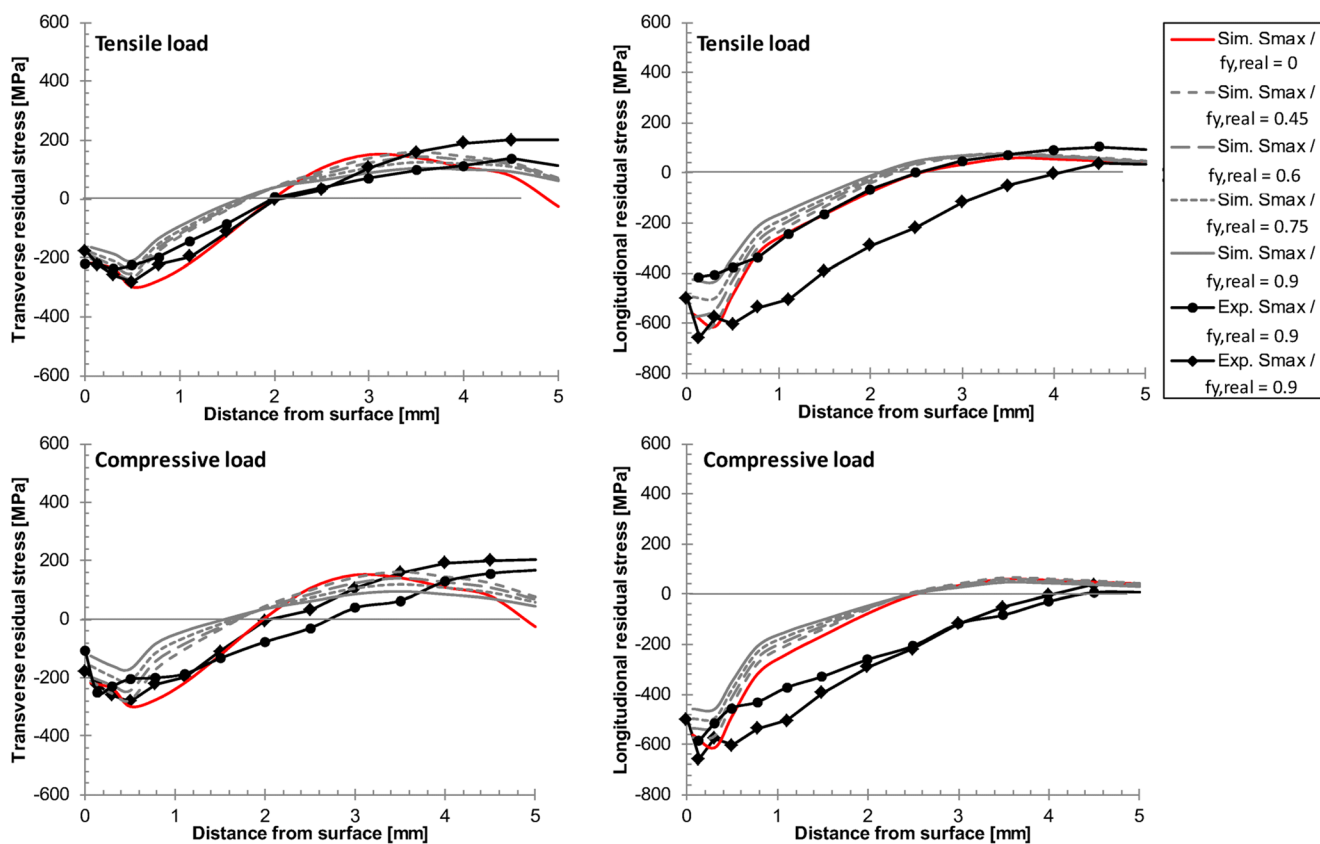

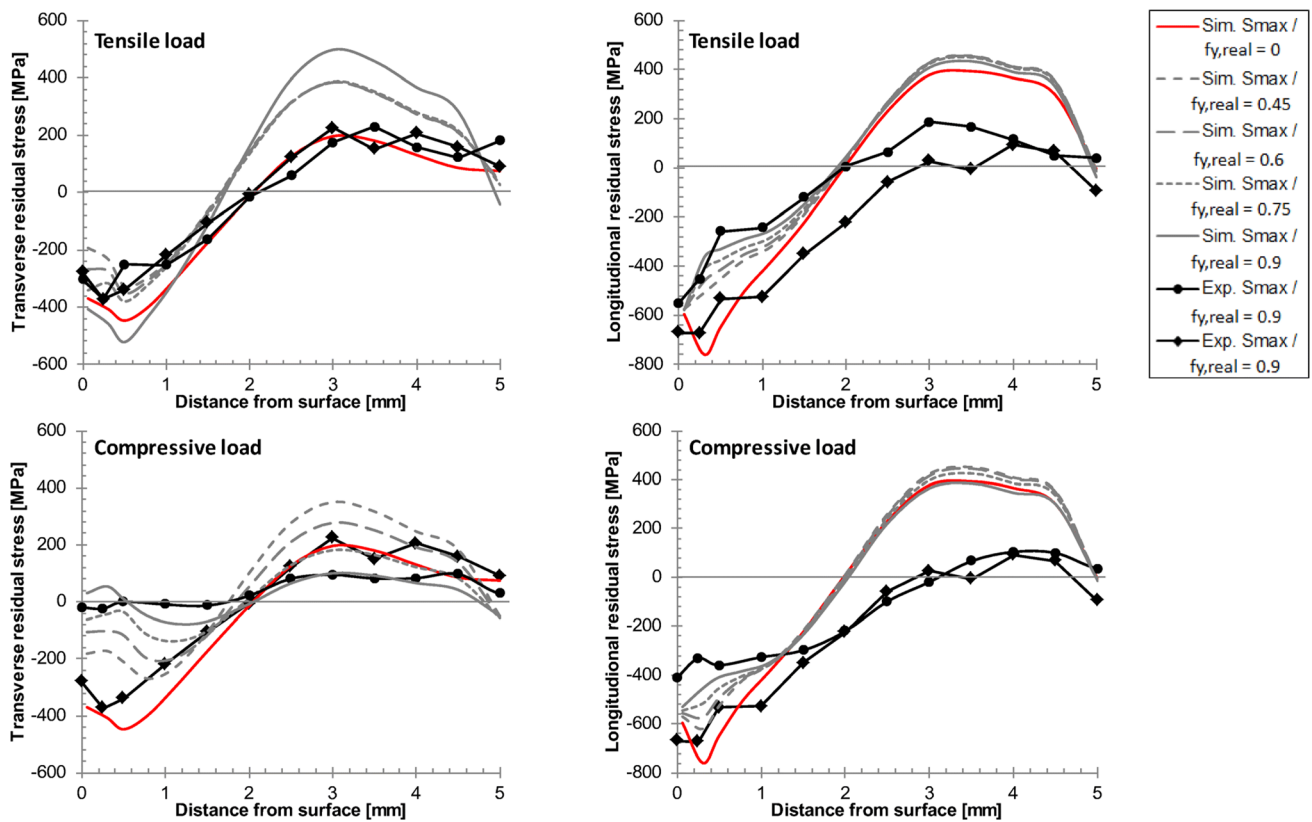**Fig. 7** Residual stress depth profiles for S355 fillet weld

Fig. 8 Residual stress depth profiles for S960 fillet weld

compressive residual stresses relax under a maximum nominal stress of $-0.6\,f_y$, as it was earlier suggested by Mikkola et al. [7]. For S355J2, however, only a slight relaxation was observed at the same normalized load level. For a nominal load level of $-0.45\,f_y$ and in accordance with Marquis et al. [5], only a slight relaxation was observed for both materials. For tensile loads on the contrary, no significant relaxation was observed by X-ray and neutron diffraction measurements,

and only a slight relaxation was determined by numerical simulation. Thus, the recommendation of $S_{max} = f_y$ [8] for tensile overloads is valid for the currently investigated welded joints.

For tensile overloads, however, it should be mentioned that the compressive residual stress is not the only factor for fatigue strength improvement. Even if full residual stress relaxation occurs at HFMI-treated welded joints, the effect of SCF
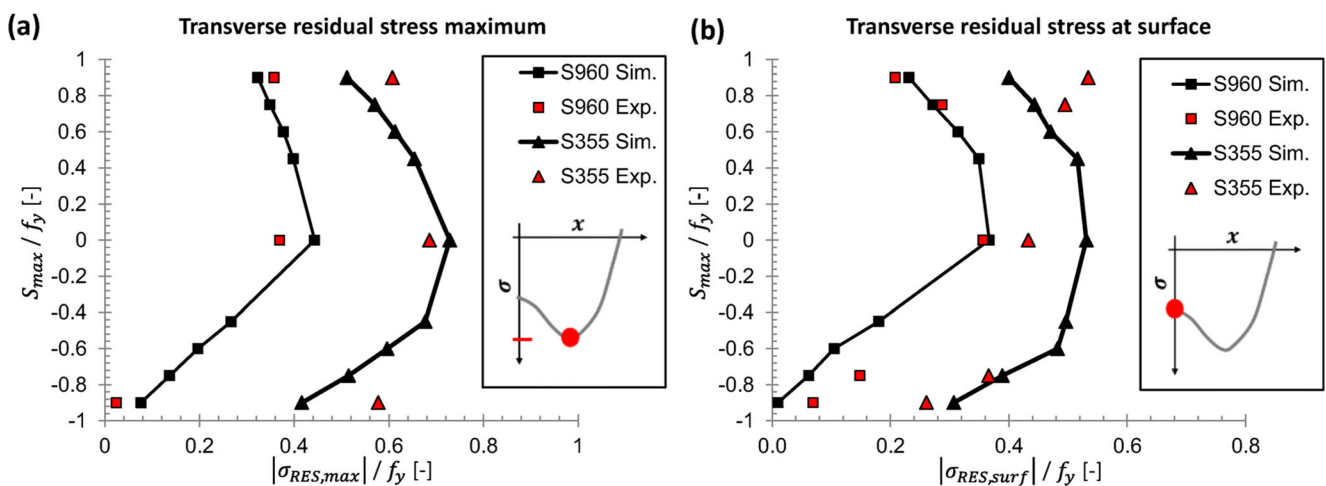

Fig. 9 a Normalized transverse residual stress maximum $|\sigma_{RES, max}|$ and **b** transverse residual stress at surface $|\sigma_{RES, surf}|$ after load with maximum nominal stress S_{max}

reduction and work hardening may still lead to a significant fatigue life extension of HFMI-treated welded joints. Thus, numerous experimental studies of HFMI-treated welded joints under variable amplitude loading [44, 45, 46] show still a significant improvement even if the maximum nominal stresses range between $0.55 f_y$ and $0.76 f_y$.

6 Conclusion

The relaxation behavior of HFMI-induced residual stresses was studied by means of X-ray and neutron diffraction techniques at transverse stiffeners made of mild S355J2 steel and high strength S960QL steel. For this, the load levels at a normalized maximum nominal stress of $\pm 0.45 f_{y, real}$, $0.6 f_{y, real}$, $0.75 f_{y, real}$, and $0.9 f_{y, real}$ were chosen. Moreover, this study was complemented by numerical simulations at the same load levels. The following conclusion could be made:

- Compressive overloads close to the base materials real yield strength $(-0.9 f_{y, real})$ lead to full residual stress relaxation for S960QL and around half residual stress relaxation for S355J2.
- For tensile overloads close to the base material $(0.9 f_{y, real})$ yield, only minor residual stress relaxation was observed for both steel grades.
- Significantly less residual stress relaxation was determined for S355J2 at the same normalized nominal stress $S_{max}/f_{y, real}$.

References

1. Barsoum Z, Marquis GB (2016) IIW Recommendation for the HFMI treatment for improving the fatigue strength of welded joints. Springer, Singapore

2. Leitner M, Ottersböck M, Pußwald S, Remes H (2018) Fatigue strength of welded and high frequency mechanical impact (HFMI) post-treated steel joints under constant and variable amplitude loading. Eng Struct 163:215–223

3. Marquis G (2010) Failure modes and fatigue strength of improved HSS welds. Eng Fract Mech 77(11):2051–2062

4. Schulze V (2006) Modern mechanical surface treatment: states, stability, effects. Wiley VCH, New York

5. Marquis GB, Mikkola E, Yildirim HC, Barsoum Z (2013) Fatigue strength improvement of steel structures by high-frequency mechanical impact: proposed fatigue assessment guidelines. Weld. World 57(6):803–822

6. Haagensen PJ, Maddox SJ (2013) *IIW recommendations on post weld improvement of steel and aluminium structures*, no. 79. Woodhead Publishing Ltd, Cambridge

7. Mikkola E, Remes H (2017) Allowable stresses in high-frequency mechanical impact (HFMI)-treated joints subjected to variable amplitude loading. Weld World 61(1)

8. Kuhlman U, Breunig S, Ummenhofer T, Weidner P (2018) ntwicklung einer DASt-Richtlinie für höherfrequente Hämmerverfahren - Zusammenfassung der durchgeführten Untersuchungen und Vorschlag eines DASt-Richtlinien-Entwurfs (in German). Stahlbau 10(87)

9. Manteghi S, Maddox SJ (2004) Methods for fatigue life improvement of welded joints in medium and high strength steels, Int Inst Weld, p. IIW Document XIII-2006-04

10. Huo L, Wang D, Zhang Y (Jan. 2005) Investigation of the fatigue behaviour of the welded joints treated by TIG dressing and ultrasonic peening under variable-amplitude load. Int J Fatigue 27(1):95–101

11. McCLUNG RC (Mar. 2007) A literature survey on the stability and significance of residual stresses during fatigue. Fatigue Fract Eng Mater Struct 30(3):173–205

12. Farajian-Sohi M, Nitschke-Pagel T, Dilger K (Jan. 2010) Residual stress relaxation of quasi-statically and cyclically-loaded steel welds. Weld World 54(1–2):R49–R60

13. Leitner M, Khurshid M, Barsoum Z (Jul. 2017) Stability of high frequency mechanical impact (HFMI) post-treatment induced residual stress states under cyclic loading of welded steel joints. Eng Struct 143:589–602

14. Schubnell J, Discher D, Farajian M (2019) Static, dynamic and cyclic properties of the heat affected zone for different steel grades. Mater Test 61(7)

15. T. Nitschke-Pagel, K. Dilger, H. Eslami, I. Weich, and T. Ummenhofer, "Residual stresses and near-surface material condition of welded high strength steels after different mechanical post-weld treatments," 2010

16. Wimpory RC, Mikula P, Šaroun J, Poeste T, Li J, Hofmann M, Schneider R (Jan. 2008) Efficiency boost of the materials science diffractometer E3 at BENSC: one order of magnitude due to a horizontally and vertically focusing monochromator. Neutron News 19(1):16–19

17. Webster PJ, Mills G, Wang XD, Kang WP, Holden TM (Jul. 1996) Impediments to efficient through-surface strain scanning. J Neutron Res 3(4):223–240

18. Vrána M, Mikula P (2005) Suppression of surface effect by using bent-perfect-crystal monochromator in residual strain scanning. Mater Sci Forum 490–491:234–238

19. Use of symmetry for residual stress determination, 2018, pp. 9–14

20. Eigenmann B, Macherauch E (Mar. 1995) Röntgenographische Untersuchung von Spannungszuständen in Werkstoffen. Materwiss Werksttech 26(3):148–160

21. Hemmesi K, Farajian M, Boin M (Jul. 2017) Numerical studies of welding residual stresses in tubular joints and experimental validations by means of x-ray and neutron diffraction analysis. Mater Des 126:339–350

22. Hardenacke V, Farajian M, Siegele DD (2015) Modelling and simulation of high frequency mechanical impact (HFMI) treatment of welded joints, In: 68th IIW annual assembly

23. Foehrenbach J, Hardenacke V, Farajian M (2016) High frequency mechanical impact treatment (HFMI) for the fatigue improvement: numerical and experimental investigations to describe the condition in the surface layer. Weld World 60(4):749–755

24. Schubnell J, Hardenacke V, Farajian M (2017) Strain-based critical plane approach to predict the fatigue life of high frequency mechanical impact (HFMI)-treated welded joints depending on the material condition. Weld World 61(6)

25. Ernould C, Schubnell J, Farajian M, Maciolek A, Simunek D, Leitner M, Stoschka M (2019) Application of different simulation approaches to numerically optimize high-frequency mechanical impact (HFMI) post-treatment process. Weld. World 63(3):725–738

26. Ernould C (2017) Numerical simulation of pin kinetic and its influence on the material hardening, residual stress field and topography during high frequency mechanical impact (HFMI) treatment. KIT Karlsruhe

27. Le CH (2018) Numerische Untersuchung von Approximationsformeln von Kerbformzahlen an der reallen Schweißnahtgeometrie von Quersteifen (in German). Karlsruhe Institut of Technology

28. Schubnell J et al (2018) "Influence of the optical measurement technique and evaluation approach on the determination of local weld geometry parameters for different weld types," in IIW Annual Assembly, IIW Document XIII-2735-18

29. Dassault Systemes Simulia Corp, Abaqus Documentation, Version 6.14. Providence, RI, USA, 2014

30. Maciolek A (2017) Implementierung eines elasto-viskoplastischen Materialmodells zur simulation des Kugelstrahlens an Komponenten aus 42CrMoS4 Stahl, (implementation of a elasto-viscoplastic material model of the simulation of shot peening at components of 41CrMoS4 steel). KIT Karlsruhe

31. Chaboche J-L (1986) Time-independent constitutive theories for cyclic plasticity. Int J Plast 2(2):149–188

32. Chaboche J-L (1989) Constitutive equations for cyclic plasticty and cyclic viscoplasticity. Int J Plast 5:247–302

33. Zaverl F, Lee D (1978) Constitutive relations for nuclear reactor core materials. J Nucl Mater 75(1):14–19

34. Chaboche J-L (2009) Plasticity and viscoplasticity under cyclic loadings. Nonlinear Comput Mech 3:1–60

35. Erz A, Klumpp A, Hoffmeister J, Schulze V (2012) Numerical Simulation of Micropeening of quenched and tempered AISI 4140, In: Proceedings of the 12th International Conference on Shot Peening (ICSP-12), pp. 352–358

36. Armstrong PJ, Frederick CO (1966) A mathematical representation of the multiaxial Bauschinger effect

37. Frederick CO, Armstrong PJ (2007) A mathematical representation of the multiaxial Bauschinger effect. Mater High Temp 24(1):1–26

38. Schubnell J, Eichheimer C, Ernould C, Maciolek A, Rebelo-Kornmeier J, Farajian M (2019) Investigation of the Coverage for High Frequency Mechanical Impact (HFMI) Treatment of different Steel Grades. Int J Process Technol, (accepted)

39. Saunders N, Miodownik P (1998) CALPHAD (calculation of phase diagrams): a comprehensive guide. Pergamon

40. Sarmast A, Schubnell J, Farajian M (2019) An numerical investigation on the effect of multi-layer repair welding on temperature history and residual stresses of S960 and S355 weldments. In: ESI forum Germany

41. Hobbacher A (2009) Recommendations for fatigue design of welded joints and components. Welding Research Council, New York

42. Macherauch E, Wohlfahrt H (1985) Eigenspannungen und Ermüdung. Ermüdungsverhalten metallischer Werkstoffe, Residual stresses and fatigue. Fatigue behavior of metal components (in German). In: Ermüdungsverhalten metallischer Werkstoffe, fatigue of metallic materials (in German). DGM Informationsgesellschaft Verlag GmbH, Oberursel, pp 237–283

43. Löhe D, Lang K-H, Vöhringer O (2002) Residual stress and Fatigue Behavior. In: Totten G, Howes M, Inoue T (eds) Handbook of Residual Stress and Deformation of Steel, 1st edn. ASM International

44. Vanrostenberghe S et al (2015) Improving the fatigue life of high strength steel welded structures by post weld treatments and specific filler material (FATWELDHSS). Luxembourg

45. Nykänen T, Marquis GB, Björk T (2009) A simplified fatigue assessment method for high quality welded cruciform joints. Int J Fatigue 31(1):79–87

46. Yildirim HC, Marquis GB (2013) A round robin study of high-frequency mechanical impact (HFMI)-treated welded joints subjected to variable amplitude loading. Weld. World 57(3):437–447